Science Advances

Protein detection in blood with single-molecule imaging – August 11, 2021

Abstract

The ability to characterize individual biomarker protein molecules in patient blood samples could enable diagnosis of diseases at an earlier stage, when treatment is typically more effective. Single-molecule imaging offers a promising approach to accomplish this goal. However, thus far, single-molecule imaging methods have not been translated into the clinical setting. The detection limit of these methods has been confined to the picomolar (10^{-12} M) range, several orders of magnitude higher than the circulating concentrations of biomarker proteins present in many diseases. Here, we describe single-molecule augmented capture (SMAC), a single-molecule imaging technique to quantify and characterize individual protein molecules of interest down to the subfemtomolar ($<10^{-15}$ M) range. We demonstrate SMAC in a variety of applications with human blood samples, including the analysis of disease-associated secreted proteins, membrane proteins, and rare intracellular proteins. SMAC opens the door to the application of single-molecule imaging in noninvasive disease profiling.

INTRODUCTION

Diseased cells release biomarker proteins into the bloodstream (*1*). These proteins can be tissue-specific but normal in structure, contain mutated regions, or carry abnormal secondary modifications. Conventional blood tests, such as the enzyme-linked immunosorbent assay (ELISA), typically cannot discern protein concentrations below the picomolar (10^{-12} M) range (*1*). The circulating levels of biomarker proteins associated with early stages of common disorders such as cancer or infection frequently fall in the femtomolar (10^{-15} M) range and below (*2*, *3*). Newer methods—including digital ELISA (*4*), DNA biobarcoding (*5*), proximity ligation (*6*, *7*), and immuno-polymerase chain reaction (immuno-PCR) (*8*, *9*)—have been developed to improve the sensitivity of protein assays to the femtomolar range. However, these tests rely on enzymatic amplification and ensemble measurements of the target molecule (*1*). Ensemble methods are limited by detection errors from background or nonspecific reagent binding, especially in complex clinical fluids such as blood.

Single-molecule imaging approaches visualize individual protein molecules, providing greater sensitivity, reliability, and depth of information than ensemble methods (*10*). The detection limit of single-molecule imaging approaches has thus far reached the picomolar range in cell lysates (*11*, *12*). However, single-molecule imaging of proteins in the blood has not been previously achieved. Here, we describe single-molecule augmented capture (SMAC), a technique that allows quantification of individual protein molecules in the blood down to the subfemtomolar range. SMAC offers orders of magnitude greater detection sensitivity and specificity than other single-molecule imaging methods, opening up the possibility of quantifying and characterizing disease-associated molecules in patient samples at the single-molecule level. SMAC interrogates images formed by individual target protein molecules within biological samples and uses a fluorescence shape recognition algorithm to correct detection errors derived from nonspecific antibody absorption or autofluorescence in complex biological fluids. Thus, true signals are reliably distinguished from false background signals in samples. Here, we demonstrate a wide variety of applications of SMAC in blood-based human disease profiling.

RESULTS

In SMAC, individual proteins of interest are continuously pulled down by a capture antibody on a microfluidic device, probed by a fluorophore-labeled detection antibody, and visualized by single-molecule imaging (Fig. 1A). We achieved subfetomolar sensitivity by implementing the following strategies (Fig. 1B). First, we created the SMAC chip, a highly efficient target-capture microfluidic device (Fig. 1A). The chip has the following features: (i) It is coated with a dense layer of multivalent, biotinylated antibody via a NeutrAvidin linker (*12*, *13*), which enhances capture affinity and suppresses nonspecific binding; (ii) the total capture area of the chip is minimized, which concentrates proteins of interest by $>10^4$-fold; and (iii) a staggered herringbone micromixer roof (*14*) and oscillating sample flow scheme are incorporated onto the chip, which promote target-antibody collisions (Fig. 1B and fig. S1, A and B). Second, we used a flow

cytometry–based antibody screening process to rapidly identify the best capture/detection antibody pairs for target proteins (fig. S1, C and D). Third, we acquired time-stream–averaged total internal reflection fluorescence (TIRF) images to resolve spatially individual fluorescent spots of target protein molecules (fig. S2, A and B; see Materials and Methods for details). Time stream TIRF microscopy helps overcome diffusive background from autofluorescent substances in test samples and in the microfluidic device itself. These autofluorescent substances dissociate rapidly from the chip surface and photobleach more quickly than fluorophore-labeled detection antibodies. By contrast, detection antibodies specifically bound to target protein molecules remain attached to the chip for a longer time (fig. S2C). Thus, by time-averaging an imaging stream, SMAC removes autofluorescent background signals while preserving specific signals from detection antibodies (fig. S2, A and B).

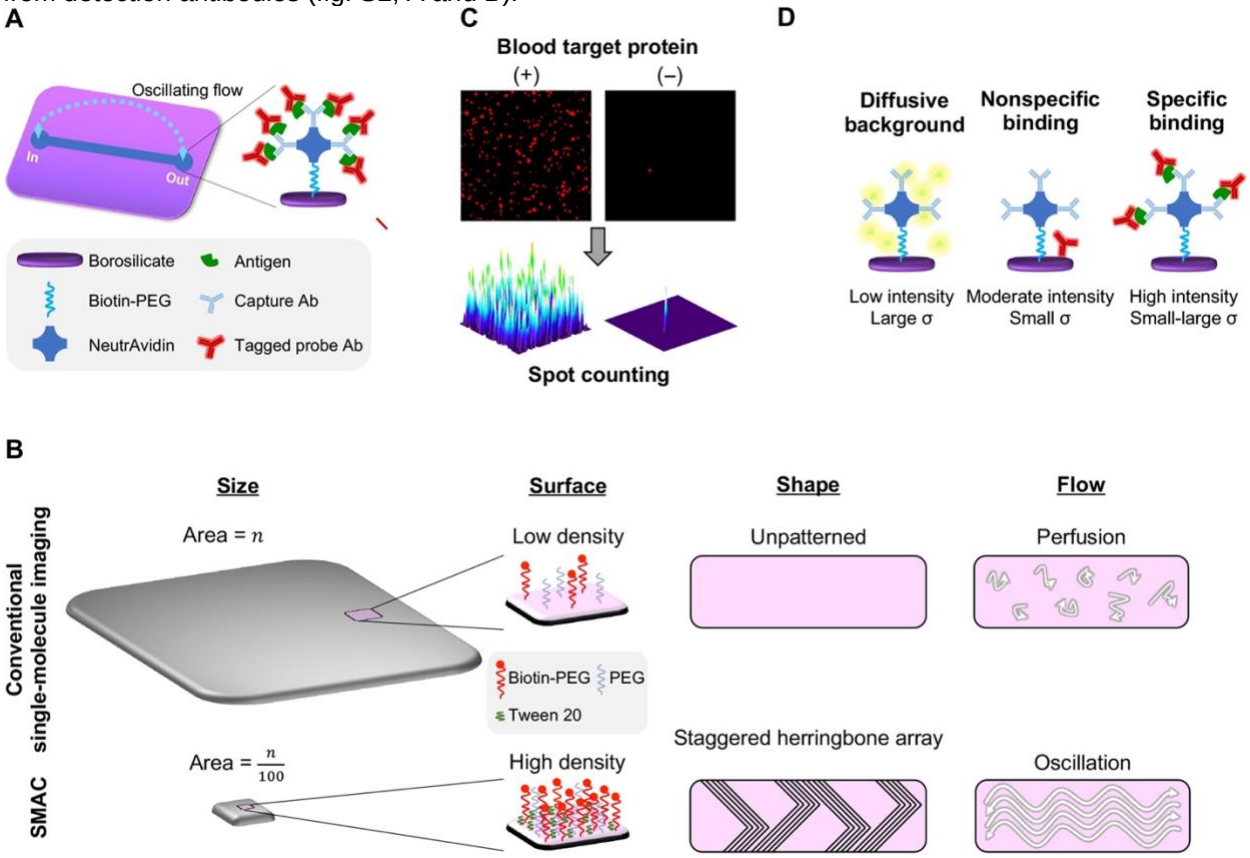

Fig. 1. SMAC chip design.
(**A**) Schematic diagram of the SMAC platform. Proteins of interest were pulled down as clusters via continuous oscillating flow on a multivalent microfluidic device and then probed with fluorophore-labeled detection antibody (Ab). PEG, polyethylene glycol. (**B**) Schematic diagram depicting features of SMAC (bottom), contrasted to conventional single-molecule imaging methods (top), that enable single-molecule imaging of blood samples at subfemtomolar sensitivity. The miniature size, high-density capture surface, patterned channel shape, and continuous oscillating flow scheme of the SMAC chip synergize to efficiently concentrate proteins of interest on the chip. (**C**) Target protein clusters were visualized by TIRF microscopy. (**D**) Schematic diagrams depicting different binding types that give rise to different fluorescence intensity and spot size combinations.

Last, to achieve subfetomolar sensitivity with minimal detection errors for proteins of rare occurrence in samples, we applied a “fluorescence shape” recognition algorithm (referred to as shape analysis; see Materials and Methods for details). Because NeutrAvidin and the capture antibody are multivalent (Fig. 1A), fluorophore-labeled detection antibody molecules form clusters around target protein molecules on each NeutrAvidin tetramer, generating fluorescent spots with combinations of size (measured by the σ of the Gaussian fitting of the spot) and intensity (*I*; measured in number of photons) that are distinct from those of background spots because of diffusive background and nonspecifically absorbed detection

antibody molecules (Fig. 1, C and D). We referred to these combinations of size and intensity as the *I*-σ shape (Fig. 2A). The *I*-σ shape reflects the combination of fluorescent signals emitted by specific antibody binding, nonspecific antibody binding, and background diffusive autofluorescence and can be deconvoluted into its individual components via shape analysis (Fig. 2, A and B). To perform shape analysis, we first represented the *I*-σ shape of a test sample as a two-dimensional (2D) histogram depicting the absolute number of spots in a set number of *I*-σ bins (Fig. 2C). We corrected for detection errors by subtracting out the maximum projected number of background reference spots (experimentally derived from a large pool of negative control background samples) from each bin of the test sample *I*-σ histogram (Fig. 2C). This analysis allowed us to overcome confounding effects of background signals at extremely low target protein concentrations in complex fluids such as blood.

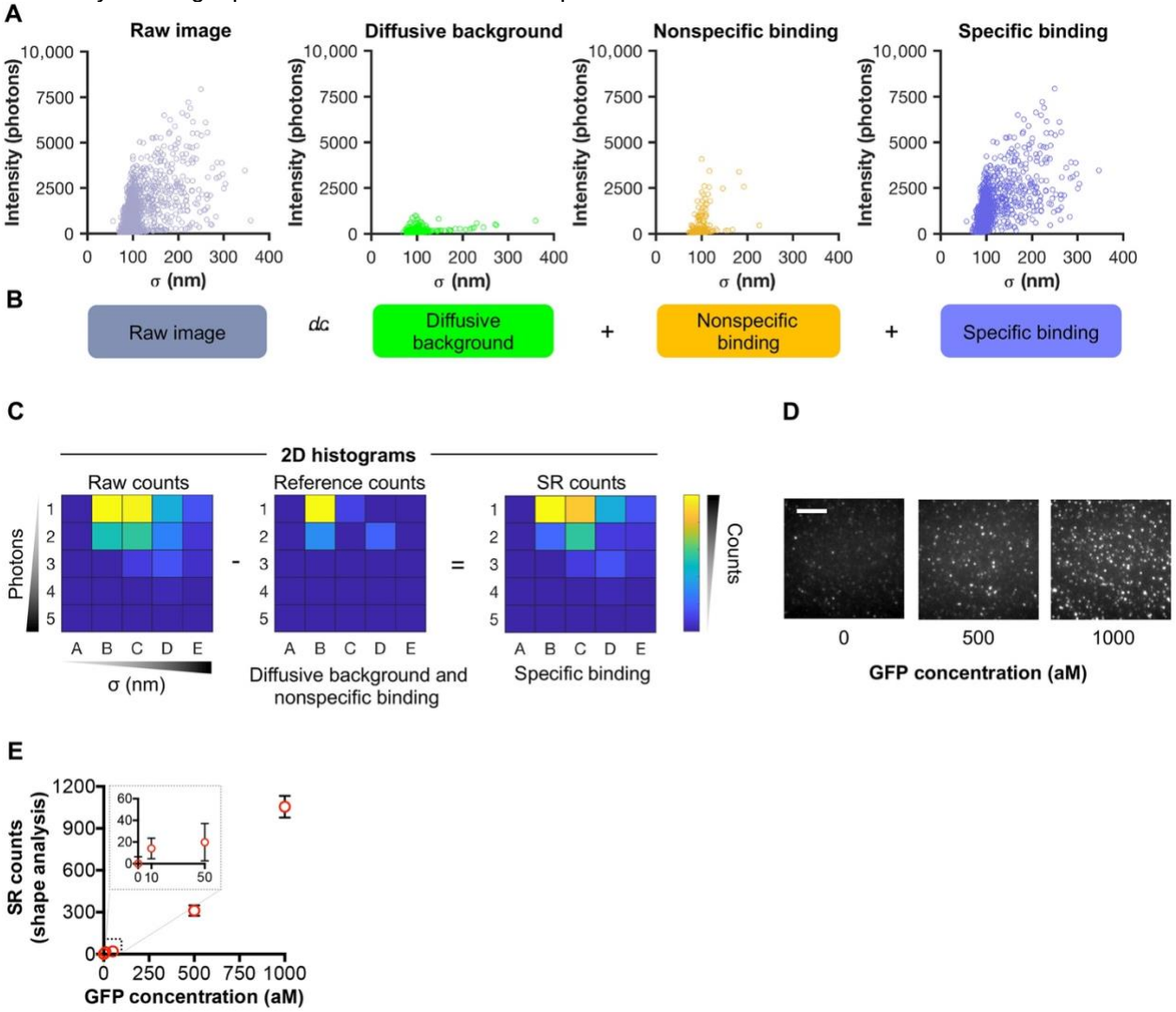

Fig. 2. SMAC and protein analysis methods.
(**A**) Schematic diagrams depicting different binding types that give rise to different fluorescence intensity and spot size combinations. Scatter plots (A) and decomposition (**B**) of spot sizes (σ) and intensities arising from different binding types after Gaussian fitting of each spot. These data were converted into a 2D histogram of intensity and σ as shown in (C). (**C**) The number of specific binding spots (SR counts) is obtained by subtracting the 2D histogram of a scaled reference histogram conveying the intensity-σ distributions of diffusive background and nonspecific binding from the 2D histogram of raw counts (see Materials and Methods for details). (**D**) Representative SMAC images of purified GFP molecules at 500 aM and 1 fM concentrations. The intrinsic fluorescence of GFP was measured without detection antibody. (**E**) Graph illustrating the sensitivity of SMAC with shape analysis (SR counts) using purified GFP from 10 aM to 1 fM. Data are expressed as means ± SD. Scale bar, 4 μm.

OPEN IN VIEWER

We first validated the design of SMAC using a capture antibody targeting purified green fluorescent protein (GFP). Because GFP is intrinsically fluorescent, we did not use a detection antibody. By applying the shape recognition algorithm, we achieved a limit of detection (LOD) of 61 aM GFP (Fig. 2, D and E, and fig. S3A). This detection sensitivity is >10^4-fold more sensitive than ELISA and existing single-molecule imaging approaches (fig. S3B) (*11*, *12*). Note that for samples containing proteins of relatively high abundance, such as >10 fM GFP, it is not necessary to use the shape-recognition algorithm. Instead, we measured the overall fluorescence intensity per sample (referred to as integrated intensity analysis) by adjusting the EMCCD (electron multiplier charge-coupled device) camera gain such that the signal would fall within the linear range of the camera. We then compensated the image signal level using the corresponding electron-multiplying (EM) gain and a standard calibration curve (see Materials and Methods for details), allowing us to accurately detect GFP from subfemtomolar concentrations up to 100 nM in a single sample without the need for dilution (fig. S3A), which corresponds to a dynamic range of around nine orders of magnitude (compared to approximately two orders of magnitude for ELISA).

Next, we developed SMAC to detect a disease-associated secreted protein, prostate-specific antigen (PSA), as a proof of principle for the application of SMAC to clinical samples (Fig. 3). PSA is a well-established biomarker for prostate cancer (*15*–*18*). While the normal prostate gland constitutively produces PSA, the expression of this protein is often dysregulated in prostate cancer cells, leading to either elevated or reduced PSA levels in the blood (*15*–*18*). SMAC could detect purified PSA at an LOD of 648 aM (Fig. 3, B and C), 10^5 times below the limit of the current clinical PSA test (fig. S4B) (*4*), and is comparable to the reported limit of digital ELISA (*4*). SMAC was able to detect PSA in lysate derived from a single prostate cancer cell titrated into aqueous buffer or human blood (Fig. 3, D to F). Furthermore, the SMAC PSA assay achieved a dynamic range of more than six orders of magnitude (from 5 fM to >1 nM) (fig. S4A) compared to two orders of magnitude for the clinical PSA test.

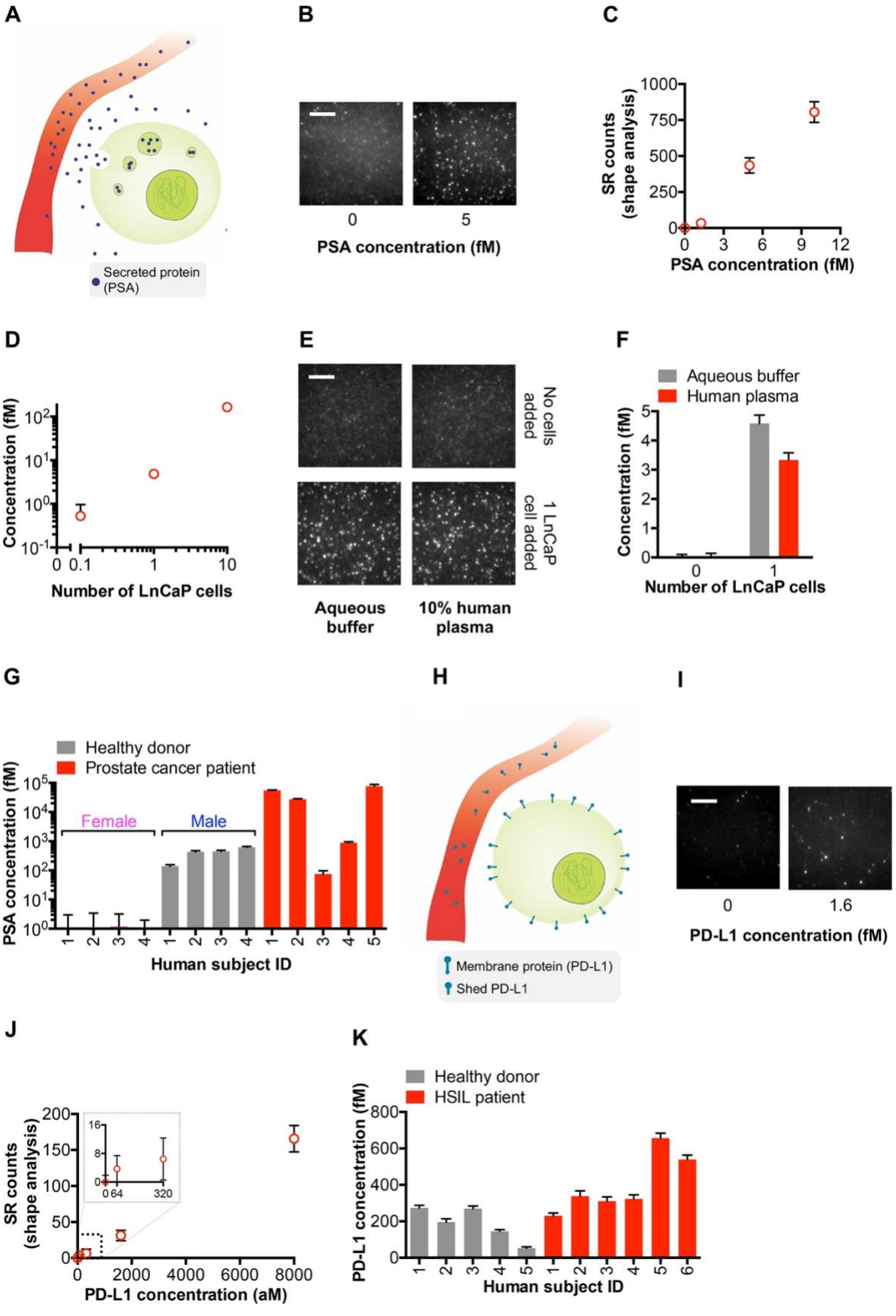
A
Secreted protein (PSA)
B
0
5
PSA concentration (fM)
C
SR counts (shape analysis)
1000
750
500
250
0
0 3 6 9 12
PSA concentration (fM)
D
Concentration (fM)
10^2
10^1
10^0
10^{-1}
0 0.1 1 10
Number of LnCaP cells
E
No cells added
1 LnCaP cell added
Aqueous buffer
10% human plasma
F
Aqueous buffer
Human plasma
Concentration (fM)
5
4
3
2
1
0
0 1
Number of LnCaP cells
G
Healthy donor
Prostate cancer patient
PSA concentration (fM)
10^5
10^4
10^3
10^2
10^1
10^0
Female
Male
1 2 3 4 1 2 3 4 1 2 3 4 5
Human subject ID
H
Membrane protein (PD-L1)
Shed PD-L1
I
0
1.6
PD-L1 concentration (fM)
J
SR counts (shape analysis)
200
150
100
50
0
16
8
0
0 64 320
0 2000 4000 6000 8000
PD-L1 concentration (aM)
K
Healthy donor
HSIL patient
PD-L1 concentration (fM)
800
600
400
200
0
1 2 3 4 5 1 2 3 4 5 6
Human subject ID

Fig. 3. Detection of secreted and membrane proteins in blood by single-molecule imaging.
(**A**) Schematic diagram of secreted PSA release from a tumor cell (lime) into a blood vessel (red). SMAC images (**B**) and shape analysis (**C**) of purified human PSA at femtomolar concentrations in aqueous buffer. (**D**) Quantification of PSA in lysate from different numbers of human prostate cancer cells (LnCaP) added into aqueous buffer. SMAC images (**E**) and quantification of PSA (**F**) in lysate from one LnCaP cell in either aqueous buffer or human plasma. (**G**) PSA levels in the blood of patients with prostate cancer (n = 5) and healthy male (n = 4) and female (n = 4) control blood donors. (**H**) Schematic diagram of membrane-bound programmed death-ligand 1 (PD-L1) release from a tumor cell (lime) into a blood vessel (red). SMAC images (**I**) and shape analysis (**J**) of purified human PD-L1 at femtomolar concentrations in aqueous buffer. (**K**) Quantification of circulating PD-L1 levels in patients with high-grade squamous intraepithelial lesions (HSILs; n = 6) and healthy donors (n = 5). PSA data and PD-L1 data are expressed as means ± SD. Scale bars, 4 μm.
OPEN IN VIEWER

To test whether SMAC could monitor circulating PSA in human blood samples, we measured PSA levels in plasma samples from patients with prostate cancer (table S1) and from control healthy male and female blood donors (Fig. 3G). We found that, in most cases, SMAC detected circulating PSA in patients with prostate cancer at abnormally high levels (~10 to 100 pM) compared to baseline PSA levels in healthy male donors (~100 fM) (Fig. 3G). In contrast, conventional ELISA required >10-fold greater plasma volume to detect circulating PSA from patients with prostate cancer and could not detect basal PSA levels in control male blood donors (fig. S5), which is consistent with prior studies (*4*). We also found that one patient with prostate cancer had abnormally low circulating PSA levels (Fig. 3G and fig. S5); it has been observed that ~10% of patients with prostate cancer have very low circulating PSA levels (*19*–*21*), which correlates with poor prognosis (*22*). These results illustrate the clinical utility of SMAC for established, secreted biomarkers and demonstrate the first single-molecule imaging–based blood test, paving the way to applications of single-molecule imaging in noninvasive profiling of disease-associated proteins.

We next used SMAC to characterize membrane-bound proteins shed into the blood. Programmed death-ligand 1 (PD-L1) (*23*) is a membrane-bound immune checkpoint mediator that inhibits immune responses in a variety of disorders spanning from cancer to infection (*24*–*26*) and has recently been found in human blood (*27*, *28*). PD-L1 antagonists have shown promise in treating chronic virus infection (*29*) and multiple cancer types (*30*, *31*). A noninvasive approach to predict likelihood of benefit from immune checkpoint blockade could help tailor clinical management to individual patients (*32*). We thus used SMAC to determine the level of circulating PD-L1 in human blood (Fig. 3H).

We first developed SMAC to detect purified PD-L1 down to attomolar concentrations (LOD of 607 aM) and with a six-log dynamic range (Fig. 3, I and J, and fig. S6A). By comparison, the detection limit of conventional ensemble methods such as ELISA was 10^4-fold higher (~10 pM) and had a two-log dynamic range (fig. S6B). We next applied SMAC to characterize circulating PD-L1 molecules in patients with a chronic virus infection–induced disease: human papillomavirus (HPV)–associated cervical high-grade squamous intraepithelial lesions (HSILs; table S2) (*33*). Baseline circulating PD-L1 levels spanned from 50 to 300 fM in control blood donors (Fig. 3K). By contrast, five of six patients with HSIL had blood PD-L1 levels >300 fM, and two of these patients had levels >500 fM (Fig. 3K). By comparison, ELISA could detect circulating PD-L1 in only one of the six patients with HSIL (fig. S7). Circulating PD-L1 was likely increased in a subset of patients with HSIL because HPV infection and T cell–mediated local inflammation together induce tissue PD-L1 gene expression (*34*). The heterogeneity in PD-L1 levels is consistent with previously reported percentages of ectopic PD-L1 expression in tissue from HPV-associated lesions (*35*, *36*). These results introduce opportunities for single-molecule imaging to investigate the role of circulating immune checkpoint mediators and other membrane-tethered proteins in human diseases.

Having demonstrated the detection of extracellular proteins, including secreted and membrane-bound proteins, in blood using SMAC, we next turned to the detection of rare intracellular proteins shed from disease sites into the blood. Current blood tests target extracellular proteins as they are easily accessible (*37*), but many of these proteins are also found in the blood of healthy people (*38*). In contrast, certain intracellular proteins, particularly those that promote oncogenic transformation—such as mutant or viral oncoproteins and mutant tumor suppressor proteins—are exclusively expressed by diseased cells and hence would be more accurate biomarkers than extracellular proteins. While we and others have observed the release of intracellular proteins from cultured cancer cells (fig. S8A) (*39*), their presence in

the blood has not been reported, likely because they lie amid a plethora of other circulating proteins and are too rare to be quantified by current methods. The idea of identifying circulating intracellular proteins, such as mutant proteins, has remained an elusive goal (*40*).

We first assessed whether intracellular proteins from tumor cells are shed into the bloodstream using an animal model in which tumor cells [TC-1 (*41*)] are engineered to express cytoplasmic GFP (cytoGFP) as a prototype intracellular protein (Fig. 4A). We inoculated mice with cytoGFP$^+$ tumor cells in either subcutaneous or mucosal (buccal) tissue and were able to detect cytoGFP in the blood of these mice within 1 week after tumor challenge (Fig. 4B). The concentration of circulating cytoGFP ranged from 1 fM to 1 pM (Fig. 4B), which was in most cases below the ELISA detection limit (fig. S3B). We then induced mice with spontaneous tumor by electroporating into buccal tissue DNA vectors encoding oncogenes [*Ras*^{G12V} and *p53* short hairpin RNA (shRNA)] (*42*) and the intracellular biomarkers cytoGFP (*cyto-gfp*) and luciferase (fig. S8B). We were able to monitor the accumulation of cytoGFP in serum from these mice (from ~1 fM to ~1 nM), which paralleled tumor burden as measured by buccal luminescence imaging of luciferase activity (Fig. 4C and fig. S8C). Serum *cyto-gfp* DNA was not detectable by quantitative PCR (qPCR) even when the tumor reached >5 mm in diameter (fig. S8, D and E), likely due to the low copy number and labile nature of DNA in the blood (fig. S8F). These results are consistent with the typically low levels of circulating tumor DNA, especially in early-stage cancer (*43*, *44*). Using SMAC to follow the release of cytoGFP protein over time, we found that circulating cytoGFP levels closely mimicked luminescence imaging of tumor onset and progression (*45*) beyond week two once the initial circulating cytoGFP peak (due to electroporation-mediated tissue damage) had waned (Fig. 4D and fig. S9). These results were confirmed by cross-correlation analysis (Fig. 4E). Notably, serum cytoGFP was imperceptible by ELISA even 42 days after the tumor was induced (fig. S10). These results underscore the potential of single-molecule imaging to study fundamental disease processes in animal models and to identify rare intracellular proteins in the blood for early disease detection.

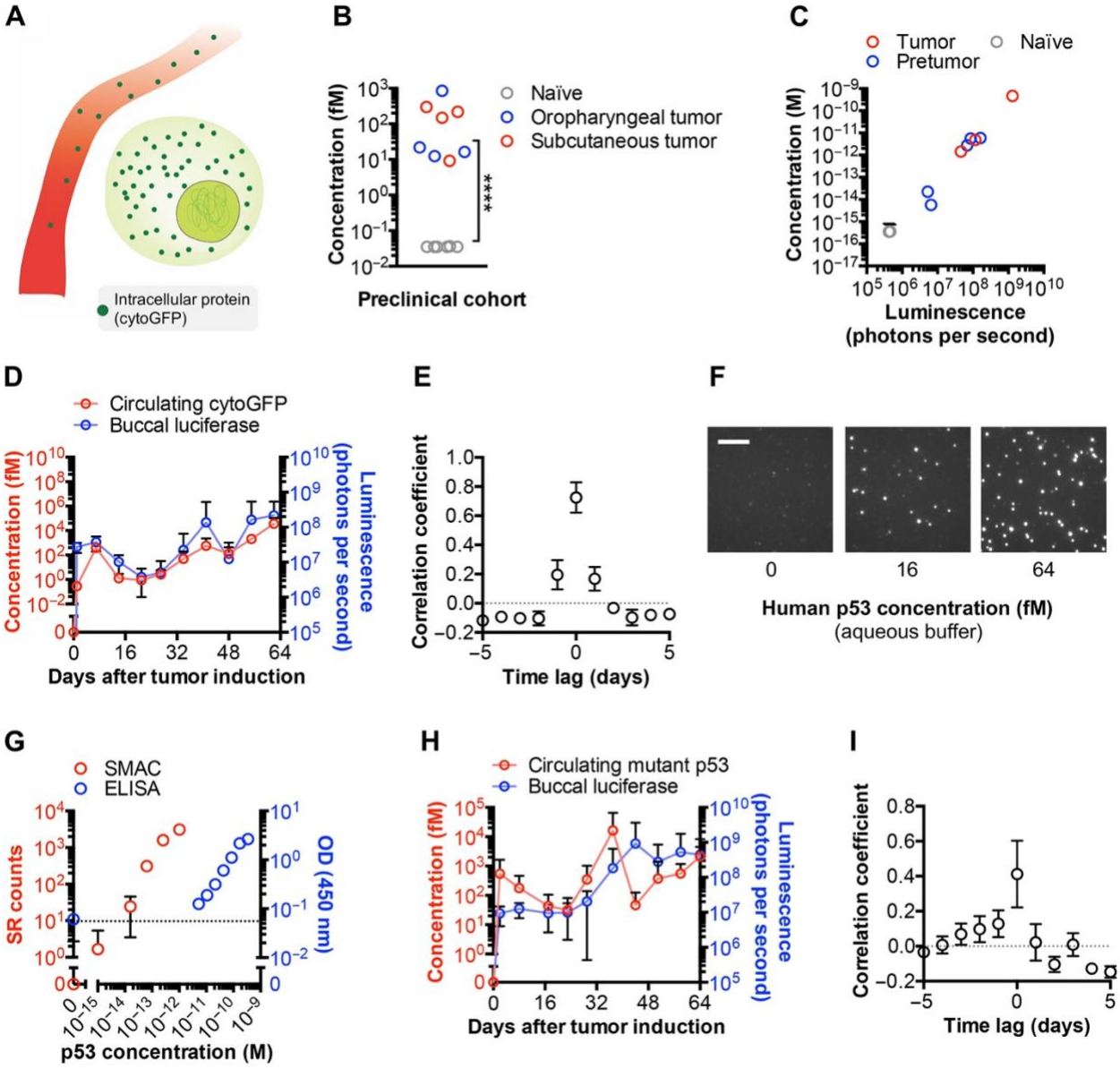

Fig. 4. Detection of cytoplasmic and nuclear proteins in blood by single-molecule imaging.
(**A**) Schematic diagram of intracellular cytoGFP release from a tumor cell (lime) into a blood vessel (red). (**B**) SMAC quantification of serum cytoGFP levels in naïve mice (gray circles; *n* = 8) and tumor-bearing mice 1 week after oropharyngeal (blue circles; *n* = 4) or subcutaneous (red circles; *n* = 4) injection of cytoGFP^{+} tumor cells (TC-1). (**C** to **E**) To induce a spontaneous cytoGFP^{+} tumor, mice (*n* = 10) were administered with DNA encoding Ras^{G12V}, p53 shRNA, cytoGFP, and luciferase. Graph depicting the relationship between tumor luciferase and serum cytoGFP concentrations assessed by SMAC at an end point of more than 2 months (C) or throughout the first 2 months (D). In (C), tumor-induced mice that displayed a grossly visible tumor were labeled “tumor” (red circles), while those that did not were labeled “pretumor” (blue circles). Using the kinetics data in (D), the time correspondence between serum cytoGFP levels and tumor burden was determined by cross-correlation analysis (E). (**F**) SMAC images of purified human p53 at femtomolar concentrations in aqueous buffer. Scale bar, 4 μm. (**G**) Comparison of the sensitivity of SMAC with shape analysis (SR counts, red circles) and ELISA [OD_{450nm} (optical density at 450 nm), blue circles] using purified human p53. The dotted line indicates the ELISA detection limit. (**H** and **I**) To stimulate a spontaneous tumor carrying mutant human p53, mice (*n* = 10) were administered with DNA encoding human p53^{R175H}, Ras^{G12V}, and luciferase. Time-course (H) and cross-correlation (I) plots depicting the relationship between tumor luciferase and serum mutant p53 levels measured by

SMAC. For cross-correlation plots, each unit time lag is around 5 days. All data are expressed as means ± SD. ****$P < 0.0001$. P values are from a two-sided unpaired t test.

OPEN IN VIEWER

To investigate the release of rare intracellular proteins in a clinically important system, we focused on the transcription factor p53 since it is a well-established tumor suppressor and the most commonly altered protein in human cancers (*46*). We developed SMAC to detect femtomolar levels of purified human p53 protein in an aqueous buffer (LOD of 12 fM), ~10^4-fold below the ELISA limit (Fig. 4, F and G). In cancer cell lines carrying different mutant p53 variants, we detected substantial levels of p53; by contrast, we detected essentially no p53 in cell lines with wild-type p53 (fig. S11A). These results reflect the enhanced stability of mutant p53 relative to wild-type p53, as the latter undergoes rapid degradation by proteasomes (*47*, *48*). Note that we used anti-p53 antibodies that theoretically recognize total p53, including wild-type and mutant variants. However, because only the mutant form of p53 is detectable in cell lines, in subsequent experiments, we interpreted the presence of p53 in samples as “mutant pattern” p53. We were able to observe mutant p53 release into the extracellular milieu from as few as 300 human ovarian cancer cells (OVCAR3) cultured overnight (fig. S11B).

We optimized SMAC with shape analysis to correct background signals for p53 spiked into serum (fig. S11C). To characterize mutant p53 proteins shed into the bloodstream in an animal model, we induced tumor formation in mice by codelivery of DNA encoding human mutant $p53^{R175H}$, Ras^{G12V}, and luciferase into the buccal mucosa using electroporation. We measured serum mutant p53 proteins in these mice over time by SMAC with shape analysis. Circulating mutant p53 levels rose in parallel with tumor progression (from ~75 fM 2 weeks after tumor onset to ~2 pM after 2 months), even in the case of tumor metastasis, as assessed by luminescence imaging (Fig. 4, H and I, and fig. S12, A and B).

We next used SMAC to identify mutant p53 proteins in the blood of patients with high-grade ovarian cancer (HGOC; table S3) (Fig. 5A), since the tumor from >96% of patients with HGOC contains mutations in the *TP53* gene (*49*). Using normal human plasma spiked with purified p53, we verified that SMAC with shape analysis maintained femtomolar baseline sensitivity (LOD of 35 fM) for p53 in human blood yet corrected >96% of background errors (Fig. 5, B and C, and fig. S13). We detected mutant pattern p53 molecules in ~60% of plasma samples from HGOC patients with disseminated [International Federation of Gynecology and Obstetrics (FIGO) stage III] disease (ranging from <10 fM to 1 pM) but in none of the samples from age-matched control female blood donors (Fig. 5D). We reasoned that for patients with undetectable circulating p53, host autoantibodies may have depleted p53 proteins (*50*) or blocked their capture (Fig. 5A). We therefore developed SMAC to identify autoantibodies against p53. SMAC exhibited >10^3-fold greater sensitivity than existing assays and could detect autoantibodies in picoliter (10^{-12} liters) volumes of human blood (Fig. 5, E and F). Using SMAC, we measured abundant amounts of plasma anti-p53 autoantibodies in 43% of the cohort of patients with HGOC (~10^3-fold in excess of circulating mutant p53 levels) but not from any healthy donors (Fig. 5G). The presence of circulating mutant p53 and its autoantibodies appeared anticorrelated (Fig. 5H), suggesting that host immune responses might have cleared mutant tumor antigens from the blood or that autoantibodies disrupted capture of p53 (*51*, *52*). Together, SMAC detected circulating p53 protein or abundant anti-p53 autoantibodies in 86% of patients with HGOC and in no healthy individuals (Fig. 5H).

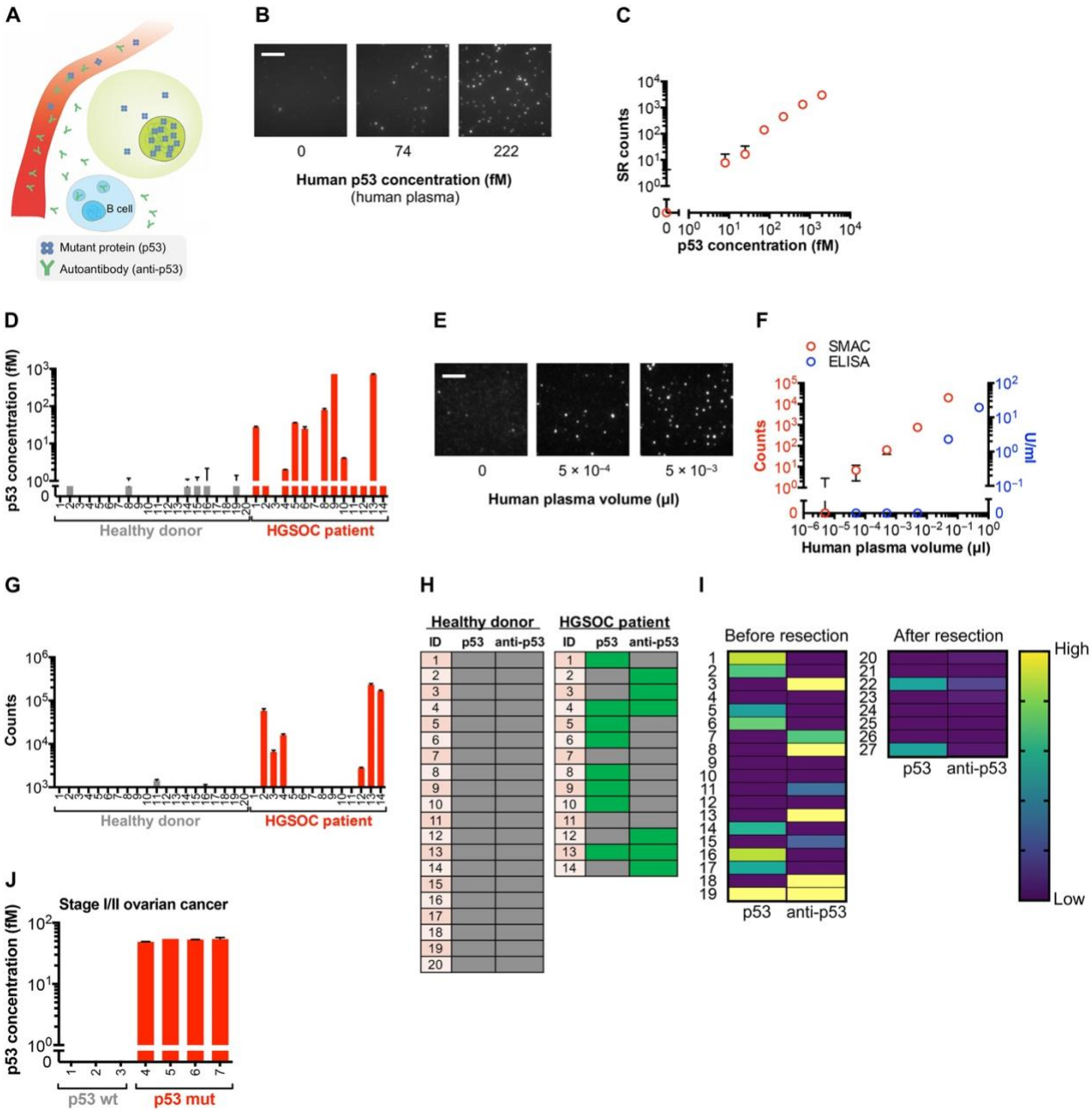

Fig. 5. Detection of circulating mutant proteins and autoantibodies in blood by single-molecule imaging. (**A**) Schematic diagram depicting release of nuclear p53 from a tumor cell (lime) and anti-p53 autoantibodies from a tumor-specific B cell (aqua) into a blood vessel (red). SMAC images (**B**) and shape analysis (**C**) of purified human p53 added at femtomolar concentrations in human plasma. (**D**) Shape analysis of circulating mutant p53 levels in plasma from patients with HGOC and healthy female blood donors. (**E**) SMAC images of endogenous anti-p53 autoantibodies in different plasma volumes, from the microliter (10^{-6} liters) to picoliter (10^{-12} liters) range, in a patient with HGOC. (**F**) Comparison of the sensitivity of SMAC (counts, red circles) and ELISA (U/ml, blue circles) using human anti-p53 autoantibodies in human plasma. (**G**) Quantification of endogenous plasma anti-p53 autoantibodies from patients with HGOC and healthy female blood donors; same cohort as in (D). (**H**) Heatmap depicting the relative levels of circulating mutant p53 or anti-p53 autoantibodies in the blood of patients with HGOC and healthy blood donors; same cohort as in (D) and (G). (**I**) Heatmap depicting the relative levels of circulating mutant p53 or anti-p53 autoantibodies in an independent cohort of FIGO stage III ovarian cancer patients with p53-mutant tumors either before or after surgical resection. (**J**) SMAC analysis of

circulating mutant p53 levels in early-stage (FIGO stage I/II) ovarian cancer patients with either p53–wild type (wt) or p53-mutant (mut) tumors. Data for individual human plasma samples (D, G, and J) are expressed as means ± SE; all other data are expressed as means ± SD. Scale bars, 4 μm.

We next characterized the levels of circulating mutant p53 and anti-p53 antibodies in an independent validation cohort of ovarian cancer patients with well-defined clinical information and p53 mutation status presenting at various pathologic stages, including early-stage (FIGO stages I and II) disease, either before or after surgical resection. These samples were from the same cohort of patients included in the recent study describing the CancerSEEK technique by Vogelstein and coworkers (*53*). Notably, the detection of ovarian cancer at an early stage, when surgical resection may be curative, remains a critical challenge in the field, as less than 20% of ovarian cancer cases are identified at stage I or II (*54*). Among ovarian cancer patients with stage III disease—all of whom carried mutant p53 within the tumor (table S4)—79% (15 of 19) had either circulating mutant p53 (8 of 19) or anti-p53 autoantibodies (8 of 19) before surgical resection (Fig. 5I and fig. S14). Only one patient had both mutant p53 and anti-p53 autoantibodies within the blood. Together, these results suggest that the presence of circulating mutant p53 and its autoantibodies is anticorrelated. Two of the four patients without circulating mutant p53 or anti-p53 autoantibodies had non–serous ovarian cancer (carcinosarcoma and undifferentiated carcinoma) (table S4). The role of p53 alterations as a driver of serous ovarian cancer has been well established (*49*), but its role in other histologic types of ovarian cancer remains unclear. Among patients with stage III ovarian cancer previously treated by surgical resection, only 25% (2 of 8) had mutant p53 in the plasma (Fig. 5I and fig. S15), suggesting that circulating mutant p53 levels serve as an index of tumor progression following therapy.

Included in the validation cohort were seven ovarian cancer patients with early-stage (stages I and II) disease (table S5). We identified circulating mutant p53 protein in four of these patients (Fig. 5J), all of whom also carried corresponding genetic alterations in *TP53* within their tumors (table S4). However, the three patients without circulating mutant p53 protein had tumors that lacked *TP53* alterations (table S4). All early-stage ovarian cancer patients with p53-mutant tumors displayed circulating mutant p53 but not anti-p53 autoantibodies, suggesting that autoantibodies have not yet formed against p53 in patients with early-stage disease. Together, these data indicate that intracellular mutant driver proteins, such as p53, are shed into the bloodstream early on in tumorigenesis, and the analysis of these proteins by single-molecule imaging, in conjunction with tissue-specific biomarkers, may facilitate earlier, more accurate detection and diagnosis of disease, when surgical resection would have more clinical benefit.

The potential applications of ultrasensitive single-molecule protein imaging extend beyond quantification of target proteins. SMAC can be used to investigate biochemical properties (e.g., secondary modifications, structural changes, and aggregation status) of individual proteins of interest within a population and unique combinations of proteins in macromolecular complexes. Because disease-associated proteins often differ between patients and healthy people not only in their total amount but also in their biochemical features, SMAC adds an extra dimension to the information obtainable from existing methods.

To explore this avenue, we developed SMAC to investigate the aggregation status of p53 complexes in test samples. Notably, certain conformational mutants of p53 have been shown to self-assemble into high-order complexes within tumor cells, and these mutants have been correlated with aggressive disease (*55*). Thus, the ability to identify these conformational p53 mutants could improve disease detection and management. To test the idea that SMAC could distinguish between conformational p53 mutants, we generated p53 mutants that have been reported to self-assemble into large complexes ($p53^{R175H}$) or remain as monomers ($p53^{L344P}$) (fig. S15A). We fused these mutants to the GFP reporter protein. We then added the recombinant mutant or wild-type p53 into buffer at different concentrations and examined them by SMAC. We found that the p53 conformational mutants produced different combinations of the number and intensities of fluorescent spots despite equal protein amounts (fig. S15, B and C). For example, at the same total p53 concentration, $p53^{L344P}$ had a large number of low intensity spots; by contrast, $p53^{R175H}$ had fewer spots, but these spots were of high intensity (fig. S15, B and C). We characterized the intensity distributions of the fluorescent spots and measured the percentage of aggregates (defined as spots greater than or equal to tetramer) in each group of conformational mutants (fig. S15, D to F). At the same p53 concentration, $p53^{R175H}$ had the largest percentage of aggregates, followed by the wild-type group and then $p53^{L344P}$ (fig. S15E). Also, the relationship between the percentage of aggregates and fluorescent spot number was different among each group of

conformational mutants (fig. S15F). We found that the aggregation-prone $p53^{R175H}$ mutant had the widest intensity distribution of fluorescent spots, followed by wild-type p53, and then the monomeric $p53^{L344P}$ mutant for a given spot number (fig. S15D). To quantify these data, we calculated the Fano factor of fluorescent p53 spots (defined as the variance in intensity divided by the mean intensity; see Materials and Methods for details) as a relative index of the aggregation status (and therefore the likely mutation status). The $p53^{R175H}$ mutant had the greatest change in Fano factor per unit change in spot number, followed by wild-type p53 and then the $p53^{L344P}$ mutant (fig. S15G). These data indicate that SMAC can reveal conformational properties of disease-associated proteins and open up the possibility of using single-molecule imaging to investigate the structural properties of mutant p53, as well as other disease-associated proteins, in clinical samples.

DISCUSSION

In this study, we describe a technology, SMAC, that improves the sensitivity of single-molecule imaging techniques by more than 1000-fold and enables direct single-molecule imaging of disease-related protein biomarkers in clinical samples. SMAC integrates an efficient microfluidic capture platform with single-molecule time stream fluorescence microscopy to achieve this unprecedented sensitivity. Moreover, we developed an error correction algorithm that minimizes background detection noise due to sample autofluorescence or nonspecific detection antibody binding. Notably, these sources of noise pose a critical obstacle in the protein diagnostics field and determine the ultimate level of sensitivity that can be reached. We report detection limits in the subfemtomolar range for multiple clinically important biomarkers, which exceeds the limits of currently used diagnostic tests by several orders of magnitude. In addition, SMAC attains a dynamic range of at least six orders of magnitude, which is exponentially greater than most existing assays. Thus, we envision SMAC as a valuable platform technology that will advance the field of noninvasive diagnostics.

We demonstrate a variety of applications of SMAC to interrogate clinically important biomarkers, such as PSA or PD-L1, in patient blood samples. We also use SMAC to identify unique classes of biomarkers, including intracellular mutant proteins. Notably, in the cancer diagnostics field, virtually all currently assessed biomarkers are extracellular proteins, and the presence of intracellular biomarkers (such as mutant transcription factors or dysfunctional signaling complexes) remains largely unexplored. Although rare, these mutant or dysregulated intracellular biomarkers likely represent much more specific disease biomarkers because they play crucial functional roles in disease pathogenesis. We found that intracellular tumor-derived proteins are released into the blood at an early stage in cancer formation and accumulate in the systemic circulation as the disease progresses. Therefore, these biomarkers may be useful both for early detection and for disease monitoring. The mechanisms by which intracellular proteins are shed from tumor cells into the blood remain unknown but may be related to a combination of accelerated cellular turnover (*56*–*60*) and active secretion, as has been documented in in vitro studies (*39*).

We discovered that a key mutant transcription factor, p53, is found in the blood of ovarian cancer patients with as early as stage I disease. Notably, detection of circulating p53 coincides with the presence of mutant p53 DNA within tumor tissue, as assessed by next-generation sequencing. We identified circulating p53 in stage I/II ovarian cancer patients with corresponding alterations in p53 DNA, but not in patients with wild-type p53. Furthermore, we observed that, in general, no circulating p53 was identified in patients with stage III/IV disease who produced anti-p53 antibodies, hinting that these antibodies may clear mutant p53 from the bloodstream.

While it introduces single-molecule imaging into the clinical arena and serves as a powerful tool for disease profiling, there are limitations of the SMAC system in its present form. First, the TIRF microscope imaging is performed sequentially, with a total acquisition time of approximately 5 min per sample. Thus, the scale at which samples can be run is currently limited. Second, for target proteins that are disease-specific and absent in control samples (such as mutant tumor proteins), control plasma from healthy blood donors can be used in the data analysis algorithm to normalize for background fluorescence in the blood (such as from substances that cause autofluorescence or nonspecific detection antibody binding). However, for target proteins that are also present to varying degree in control samples, such as tumor-associated proteins, buffer solution (rather than plasma) must be used as a negative control. For these types of target proteins, the analysis algorithm is unable to separate true signal from background in plasma.

We are in the process of converting the SMAC technology into a platform that can be broadly applied in clinical practice. To achieve this, we are developing an integrated device that combines the microfluidic

handling, single-molecule imaging, and data analysis components of SMAC. The total run-time of the SMAC assay is approximately 4 hours, including target protein capture, detection antibody incubation, and single-molecule imaging, which is in line with the time required for existing protein detection methods. Furthermore, while we have found that the sensitivity of SMAC correlates with affinity of the capture/detection antibodies used, detection limits in the femtomolar and subfemtomolar range are attained with antibodies that have dissociation constants ~10 nM or lower, which can be achieved for the vast majority of target proteins with modern antibody production technologies. Thus, we believe that the SMAC platform can be readily adapted for disease detection, diagnosis, and monitoring in the clinical setting.

In summary, our results illustrate broad applications of single-molecule imaging to characterize disease-associated secreted, membrane, and intracellular proteins in the blood, opening new avenues to detect, diagnose, and study disease. Together, the insight gained from SMAC may shed light on pathologic processes, such as dysfunctional signaling pathways, gene expression networks, or immune responses unfolding within disease and point to effective therapies. The platform described here may be adapted to investigate unique biochemical, conformational, and structural features of proteins of interest in the blood. The design of SMAC can also be readily converted into multiplex and high-throughput formats to enable large-scale, single-molecule profiling of proteins in human disease.

MATERIALS AND METHODS

Materials

Polydimethylsiloxane (PDMS) elastomer for synthesis of the single-molecule microfluidic capture device was purchased from Dow Corning. Borosilicate cover glass (22 mm by 22 mm; Thermo Fisher Scientific) served as the substrate for the capture surface. Surface passivation required the following reagents: *N*-(2-aminoethyl)-3-aminopropyltrimethoxysilane (United Chemical Technologies), Alconox (Alconox Inc.), methanol (Thermo Fisher Scientific), acetic acid (Sigma-Aldrich), sodium bicarbonate (Sigma-Aldrich), biotin–methoxypolyethylene glycol–succinimidyl valerate (biotin-mPEG-SVA) molecular weight (MW) 5000 (Laysan Bio), and mPEG-SVA MW 5000 (Laysan Bio). For GFP detection, biotinylated anti-GFP antibodies (clone RQ2, MBL International) were used. For PSA detection, biotinylated (BAF1344, R&D Systems) and Alexa Fluor 488–conjugated (clone 8301, Medix Biochemica) anti-human PSA antibodies were used. For PD-L1 detection, biotinylated (BAF156, R&D Systems) and Alexa Fluor 555–conjugated (clone 28-8, Abcam) anti–human PD-L1 antibodies were used. For human p53 detection, biotinylated (BAF1355, R&D Systems) and Alexa Fluor 555–conjugated (clone E47, Abcam) anti-human p53 antibodies were used. For human p53 detection in mice, biotinylated (BAF1355) and Alexa Fluor 488–conjugated (FL-393, Santa Cruz Biotechnology) antibodies were used. For detection of human anti-p53 autoantibodies, Alexa Fluor 555–conjugated anti-human immunoglobulin G (IgG) (H+L) cross-absorbed secondary antibodies (A-21433, Thermo Fisher Scientific) were used. Purified recombinant GFP (Cell Biolabs), human PSA (R&D Systems), human PD-L1 (R&D Systems), and human p53 (R&D Systems) were used to generate standard curves. Bovine serum albumin (BSA; New England BioLabs) and polyoxyethylene (*20*) sorbitan monolaurate (Tween 20; Thermo Fisher Scientific) were used for sample wash and dilution in single-molecule experiments. ELISA for GFP, PSA, PD-L1, p53, and anti-p53 autoantibodies was performed using the GFP ELISA Kit (Cell Biolabs), the PSA Quantikine ELISA Kit (R&D Systems), the PD-L1 Quantikine ELISA Kit (R&D Systems), the p53 SimpleStep ELISA Kit (Abcam), and the MESACUP Anti-p53 Test (MBL International), respectively, according to the manufacturer's instructions.

Antibody conjugation

Antibodies were labeled with biotin or organic fluorophores via *N*-hydroxysuccinimide (NHS)–reactive ester. For biotin conjugation, antibodies (0.1 to 1 mg/ml) were incubated with 50-fold molar excess of succinimidyl-6-(biotinamido)hexanoate (NHS-LC-biotin) (Thermo Fisher Scientific) for 30 to 60 min and then isolated on 7-kDa gel filtration columns (Thermo Fisher Scientific). For dye conjugation, antibodies were precaptured on protein G magnetic beads (Thermo Fisher Scientific) and incubated with 10-fold molar excess of Alexa Fluor dye–NHS (Thermo Fisher Scientific) for 30 to 60 min. Free dye was washed out, and antibodies were further purified on 7-kDa gel filtration columns. The degree of labeling and the concentration of antibodies were measured by spectrophotometry.

Pairwise antibody screening

To select the best pair of capture and detection antibodies recognizing proteins of interest, candidate antibodies were each labeled with biotin or organic dye as described above. Pairwise combinations of these candidate antibodies were then evaluated by flow cytometry on microbeads. Biotinylated capture antibodies (1 μg) were incubated with streptavidin M-280 magnetic Dynabeads (10^5 beads per sample; Thermo Fisher Scientific) for 30 min. The beads were washed with phosphate-buffered saline (PBS) and incubated with or without purified target proteins for 30 min. Beads were washed with PBS and incubated with different dye-labeled detection antibodies (1 μg) for 30 min. These procedures were carried out in 50 μl of total volume at 25°C with constant mixing. Beads were then washed, resuspended in PBS (500 μl), and interrogated by flow cytometry on a FACSCalibur device (BD Biosciences). The capture/detection efficiency for each pair of antibodies was calculated on the basis of the shift in mean fluorescence intensity in the presence versus the absence of target proteins. Antibodies that yielded the greatest shift were considered to have superior performance.

Purification of recombinant human p53

Human p53 was generated in-house for anti-p53 autoantibody detection experiments. Plasmid encoding human p53 (hp53; Addgene) was inserted into the pET28a bacterial expression vector. *hp53* was first amplified by PCR with the following primer set: 5′-AAAGGATCCATGGAGGAGCCGCAGTCAGA-3′ and 5′-AAAGAATTCCAGGTGGCTGGAGTGAGCCC-3′. The PCR product was cloned into the Bam HI/Eco RI sites of the pET28a vector to create pET28a-hp53. This plasmid was transformed into *Escherichia coli* BL21 competent cells (Novagen). Protein expression was induced with 1 mM isopropyl-β-D-thiogalactopyranoside at 37°C for 5 hours. Bacteria were lysed, and the soluble fraction was collected. Recombinant protein was purified by affinity chromatography on Ni–nitrilotriacetic acid agarose (QIAGEN) as per the manufacturer's instructions. Purified p53 was verified by 10 to 15% gradient SDS–polyacrylamide gel electrophoresis (SDS-PAGE; Bio-Rad) and Coomassie brilliant blue (Thermo Fisher Scientific) staining, dialyzed with PBS, and stored at −80°C in PBS containing 20% glycerol.

Cells

TC-1 cells were previously generated in our laboratory and have been reported (*41*). For experiments involving cytoGFP, TC-1 cells were retrovirally transduced with a *cyto-gfp* DNA expression cassette. LnCaP human prostate cancer cells were obtained from American Type Culture Collection (ATCC). Human cells without p53 (BHK21) and with mutant p53 [CFPAC-1 (C242R), OVCAR3 (R248Q), and TOV-112D (R175H)]; cells with wild-type p53 (MCF-7 and MCF-10); and human embryonic kidney 293T cells were from ATCC. Cells were cultured in RPMI 1640 medium or Dulbecco's modified Eagle's medium (Thermo Fisher Scientific) with 10% fetal bovine serum in the absence of phenol red and maintained under 5% CO_2 atmosphere. Lysate was prepared using a commercial lysis buffer (Abcam). Briefly, cells were harvested and resuspended in lysis buffer at a stock concentration of 10^4 cells/μl. The resultant solution was centrifuged at 10,000*g* at 4°C for 10 min. The target protein concentration in the stock lysate was determined by ELISA. For single-molecule imaging experiments, lysate was diluted 10^3 to 10^5 times in "SMAC buffer" [10 mM tris-HCl (pH 8.0), 50 mM NaCl, and 0.05% Tween 20] with BSA (0.1 mg/ml). For experiments involving supernatant, conditioned medium was collected from cells cultured for 12 to 24 hours and centrifuged at 1000*g* for 5 min. The resultant supernatant was passed through 0.22-μm filters to further remove the debris. The number of viable cells was determined using an automated cytometer (Countess II, Invitrogen) with trypan blue dye exclusion.

Enzyme-linked immunosorbent assay

ELISA was performed according to the manufacturer's instructions. Briefly, plasma or cell lysate (50 μl) was added to the sample diluent (50 μl). The mixtures were then added to antibody precoated plates and incubated at room temperature for 2 hours. The plates were washed with PBS containing 0.05% Tween 20, and horseradish peroxidase (HRP)–conjugated antibodies were then added to the plate and incubated at room temperature for 2 hours. The plates were washed as above and then developed with 3,3′,5,5′-tetramethylbenzidine (TMB) substrate solution. The reaction was terminated with a stop solution containing 1 M phosphoric acid. The signals in the plates were measured at 450-nm wavelength using a microplate reader (Bio-Rad).

Mice

Six- to eight-week-old female C57BL/6 and immune-deficient athymic nude (*Foxn1*$^{-/-}$) mice were obtained from the National Cancer Institute. C57BL/6 mice were used for experiments in which tumor cells were

directly inoculated. *Foxn1*$^{-/-}$ transgenic mice were used for experiments in which a spontaneous tumor was induced by oncogene delivery. All animal procedures complied with protocols approved by the Johns Hopkins Institutional Animal Care and Use Committee and with recommendations for the proper use and care of laboratory mice.

Transplanted tumor challenge

C57BL/6 mice were injected with cytoGFP-transduced TC-1 cells (10^5 cells per animal) in the flank (subcutaneous tissue) or buccal mucosa. At 1 week after tumor challenge, whole blood was collected from the tail vein and processed into serum for downstream experiments. Tumor growth was monitored by visual inspection, palpation, and digital caliper measurement.

Spontaneous tumor induction

Foxn1$^{-/-}$ transgenic mice were injected in the buccal mucosa with a plasmid DNA cocktail encoding (i) mutant Ras^{G12V}, (ii) SB13 transposase, (iii) firefly luciferase, and (iv) either anti-p53 shRNA carrying a GFP expression cassette or mutant human $p53^{R175H}$ (10 μg of each plasmid diluted with PBS to 30 μl of total volume); plasmids were acquired from Addgene. Immediately afterward, mice received electroporation (eight pulses of 72 V, 50-ms duration, and 200-ms interval) at the injection site with an ECM830 device (BTX Online). Tumor burden was monitored over time by whole-body luminescence imaging of luciferase activity with an In Vivo Imaging System (IVIS) Spectrum device (PerkinElmer) following intraperitoneal D-luciferin (Promega) injection. At defined time points after tumor induction, whole blood was collected from the tail vein and processed into serum for downstream experiments.

Cross-correlation analysis

To characterize the time relationship between tumor progression and fluctuations in circulating target protein levels in mice, the covariance was calculated between time series of error-corrected single-molecule serum target counts and luminescence photon counts. The covariance coefficient was computed via the “xcov” function in MATLAB (MathWorks). The time lag was narrowed down to five units, with each lag unit corresponding to approximately 5 days.

Human subjects

Blood samples were obtained from volunteer patients previously diagnosed with prostate adenocarcinoma (n = 5), high-grade cervical intraepithelial lesions (n = 6), and ovarian cancer (n = 48) who underwent clinical evaluation and management at the Johns Hopkins Hospital, Baltimore, MD, USA. Descriptions of the clinical characteristics of individual patients are provided in tables S1 to S3. Human studies were approved by the Johns Hopkins University Institutional Review Board (protocol number IRB00169055). Plasma from healthy human volunteers was acquired from Innovative Research, processed from whole blood in dipotassium-EDTA (K2-EDTA; BD Biosciences).

Human plasma preparation

Whole blood was drawn from test subjects and anticoagulated with K2-EDTA. Samples were processed within 4 hours after collection. Blood samples were diluted with an equal volume of 1× Hanks’ balanced salt solution (Corning) and added slowly on top of Lymphoprep solution (15 ml; STEMCELL Technologies) in 50-ml conical tubes (Corning). Samples were centrifuged at 1200*g* for 10 min at room temperature. The top layer was harvested as plasma and stored at −80°C.

Single-molecule capture surface passivation

Borosilicate coverslips of 130- to 170-μm thickness and 22 mm by 22 mm area served as the substrate for the capture surface. Coverslips were first cleaned in 1% Alconox with sonication for 10 min, washed with Milli-Q water (Millipore) for 10 min, and dried with filtered air. Coverslips were exposed to high-power atmospheric plasma using a PE25-JW device (Plasma Etch) for 5 min for surface cleaning and activation and then immediately dipped in methanol containing 1% *N*-(2-aminoethyl)-3-aminopropyltrimethoxysilane and 5% glacial acetic acid. Coverslips were washed thoroughly with methanol and Milli-Q water and then dried with filtered air. Coverslips were conjugated with biotin-mPEG-SVA (0.3 mg) in 10 mM sodium bicarbonate (pH 8.5) for 6 hours in a sandwich arrangement. The glass surface was then conjugated with a mixture of biotin-mPEG-SVA (0.3 mg) and PEG-mSVA (16 mg, 1:50 mass ratio) for 12 hours in a sandwich arrangement. After passivation, coverslips were washed with Milli-Q water and dried as described above. Coverslips were transferred to a clean container, vacuumed, flushed with pure nitrogen, sealed with paraffin film, and stored at −20°C. Tween 20 was added into SMAC buffers during downstream experiments to further block the surface.

Microfabrication of the SMAC chip enclosure

A master template for the device enclosure was synthesized by photolithography. Briefly, a silicon wafer was rinsed with acetone and isopropanol and then dehydrated at 200°C for 15 min. The wafer was exposed to high power oxygen plasma (100 W for 3 min at 300 to 500 mtorr of oxygen pressure) using a PE II-A apparatus (Technics) to promote photoresist adhesion. SU-8 photoresist 2050 (MicroChem) was spin-coated onto the wafer to 100 μm thickness. The wafer was then soft-baked (65°/95°C) for 5 min and exposed to ultraviolet light in an EVG620 mask aligner (EVG) loaded with a mask printed at 32,512 dpi resolution (Fineline Imaging). The wafer was then hard-baked (65°/95°C) for 15 min. The first layer of the microfluidic device consisted of the main channel with side boxes, while the second layer contained arrays of staggered herringbone grooves. After all layers of photoresist were deposited, the wafer was developed under ultrasonic agitation to yield a master template for synthesis of the silicone elastomer enclosure. To produce this enclosure, PDMS elastomer was mixed with curing agent in a 10:1 ratio (by weight), poured onto the patterned wafer, degassed, and incubated at 80°C overnight. The PDMS was then removed from the master, cut into individual devices, and bored with inlet/outlet tubing holes (750 μm in diameter). The devices were washed in an ultrasonic bath with isopropanol for 20 min and then with Milli-Q water for 5 min. Devices were dried with filtered air.

Assembly of the SMAC chip

Before assembly, the uncoated side of the borosilicate coverslip was taped to an alignment guide imprinted with a 2D replica of the flow channel. An elastomer cover microfabricated with micrometer precision by photolithography to match the exact size and shape of the flow channel was then placed on the coated side of the coverslip at the position of the channel replica on the alignment guide. This cover protects the PEG/biotin-PEG layer from oxygen plasma bombardment during the assembly procedure. The coated coverslip surface with elastomer cover and PDMS enclosure were placed inside a PE-25JW plasma etcher and treated with oxygen plasma for 30 s at 40-W radio frequency power under 100 mtorr of oxygen atmosphere. The elastomer cover was removed, and PDMS devices were then sealed to the coated side of the coverslip under a stereomicroscope with the alignment guide as a reference for the channel position. The microfluidic chip was incubated at 80°C for 3 min to drive the bonding to completion.

Preparation of the SMAC chip

Reagent introduction, removal, and wash steps were performed in parallel under automated flow actuated by a multichannel peristaltic pump (Ismatec). The SMAC chip was connected to the inlet and outlet nonshrinkable Teflon tubing (internal diameter of 0.015 inch; Weico Wire and Cable) and infused with SMAC buffer {10 mM tris-HCl (pH 8.0), 50 mM NaCl, and 0.05% Tween 20]. The inclusion of Tween 20 in the SMAC buffer further blocked nonspecific protein absorption to the PDMS chamber and the capture surface. To evacuate any air trapped inside the PDMS channel, the chip was immediately degassed under vacuum for 1 min. The chip was equilibrated with SMAC buffer at a flow rate of 50 μl/min for 10 min. The chip was then incubated with NeutrAvidin (20 μl; 0.1 mg/ml; Thermo Fisher Scientific) in SMAC buffer for 10 min. The chip was washed with SMAC buffer (1 ml) at 500 μl/min and incubated for 30 min with biotinylated antibodies (2 μl; 0.1 to 1 mg/ml) in SMAC buffer with BSA (0.1 mg/ml; $SMAC^{BSA}$ buffer). The chip was then washed with $SMAC^{BSA}$ buffer (1 ml) at 500 μl/min and readied for sample circulation.

Sample circulation in the SMAC chip

Continuous oscillating flow was actuated by a multichannel bidirectional AL-8000 syringe pump (World Precision Instruments) connected to the SMAC chip via a 26-gauge 1-cc syringe (BD Biosciences). The chip was connected at the other tubing port to the sample prepared in $SMAC^{BSA}$ buffer. For oscillating flow, the blood sample was diluted to anywhere between 2 and 50% with $SMAC^{BSA}$ buffer in a final volume of 200 to 500 μl. Note that although we used 200 to 500 μl of final sample volumes in this study, the SMAC system can actually accommodate volumes up to 10 ml without substantial loss in sensitivity because of its oscillating flow scheme and efficient target capture. By contrast, most other methods are unable to reliably detect proteins in sample volumes much greater than 100 μl. The syringe pump was programmed to carry out repeated infusion/withdrawal cycles at 500 μl/min for 2 to 4 hours. Afterward, the chip was washed with $SMAC^{BSA}$ buffer (1 ml) at 500 μl/min, incubated with fluorophore-labeled detection antibodies (1 to 10 nM) for 30 min, and then washed again with SMAC buffer (1 ml) at 500 μl/min. For circulation of clinical plasma samples, the prostate cancer patient samples were diluted 50 times. HSIL patient samples were diluted two times. HGSOC patient samples were diluted two times for p53 detection

and 10^3 to 10^6 times for anti-p53 autoantibody detection. For circulation of mouse samples, serum was diluted four times. All dilutions were carried out in $SMAC^{BSA}$ buffer. For experiments involving human samples, ~10^4-fold excess IgG matched to the isotypes of the capture and detection antibodies was further added to reduce nonspecific binding.

Single-molecule TIRF microscopy

An objective-based TIRF setup was used with a PlanApo 60× oil objective (Olympus) of high numerical aperture (1.45). While acquiring data, we also used a 1.6× field lens to capture single-molecule images at ×96 total magnification. The incident laser angle was adjusted to full TIRF mode with a prism. Flow channels in the SMAC chip were identified under bright-field illumination. An imaging region of 15 μm by 15 μm was then set. An EMCCD (Andor) was programmed to capture a consecutive time stream of 500 frames with 50-ms exposure time under continuous laser excitation of 40 to 140 W/cm^2. Immediately before imaging, we measured the laser power and TIRF angles to confirm that they were consistent. After imaging each region, the stage was displaced 80 μm down the length of the channel, and imaging was performed again as above. This process was repeated until at least 10 view fields were recorded per sample. Data were acquired with custom journals written in MetaMorph software (Molecular Devices). Integrated intensity analysis. This method was used to quantify relatively abundant proteins of interest (e.g., >10 fM) across a wide dynamic range (6 to 9 logs). Single-molecule TIRF data were first recorded using a camera EM gain setting of 300. The EM gain of the camera (i.e., 300, 10, or 1) was chosen according to predefined criteria based on the standard curve for that protein. These criteria were set such that the florescence for the sample would fall within the linear range of the standard curve for that EM gain setting.

Single-molecule shape analysis

This method was used for rare proteins of interest to correct detection errors because of diffusive background and nonspecific binding. The first 50 to 100 frames of each TIRF image were initially averaged to reduce background fluorescence from compounds arbitrarily deposited on the microfluidic capture chip, as these compounds bind weakly and rapidly dissociate from the chip. We measured the total number of fluorescent spots over 10 view fields to maximize sensitivity for rare target proteins. Single-molecule data were interpreted with the ThunderSTORM plug-in in ImageJ software (*61*). In ThunderSTORM, a wavelet filter was applied to remove noise and automatically identify fluorescent spots at a constant low threshold for each sample independent of the target protein. A low threshold setting was chosen to ensure that all potential target spots were selected regardless of variations in laser illumination intensity.

The major principle behind shape analysis is that, because target proteins are pulled down as complexes by multivalent antibodies via NeutrAvidin adapters, the shape of fluorescent spots, each represented in coordinates of (*I*; measured in number of photons) and diffraction-limited spot size (measured by the σ of the Gaussian fitting of the spot), was nonidentical between real signals and false signals from diffusive and nonspecifically absorbed antibody molecules. Therefore, a raw SMAC image can be deconvoluted into its real and false (i.e., background) components. To do so, we converted each selected spot in the raw SMAC image into an *I*-σ coordinate and sorted each spot into its respective bin in a 2D *I*-σ histogram. Note that each bin *i* of this histogram contains both real and false spots, adding up to a total of T_i spots. The next step in the analysis is to determine the number of false spots in each bin. For each target protein under different conditions, we performed SMAC on control samples lacking the target protein. For experiments involving aqueous buffer and cell supernatant, $SMAC^{BSA}$ buffer and culture medium, respectively, were used as reference samples. For animal experiments, serum from naïve mice was used as reference samples. For experiments involving human blood, plasma from multiple independent healthy blood donors was used as reference samples.

The identified spots in these control images were also sorted into bins in a 2D *I*-σ histogram. Note that each bin of this reference histogram contains only false spots. By running this assay and analysis procedure on a large set of reference samples (e.g., buffer only or blood samples from many individual healthy donors), the mean ($R\mu i$) and SD ($R\mathrm{SD}i$) of the number of spots in each bin was calculated. To correct detection errors and compute the number of real spots ($C\mu i$) for each bin, the following formula was used: $C\mu i = Ti - (R\mu i + n \times R\mathrm{SD}i)$, where *n* can be adjusted to control the maximum number of projected false spots in each bin. For this study, $n = 2$ was chosen, as statistically there is a < 3% chance that the number of false spots in each bin exceeds $R\mu i + 2R\mathrm{SD}i$. The total number of real spots was reported as "SR counts," which was calculated by summing $C\mu i$ for every bin of the test sample 2D histogram. The

LOD was calculated using the following formula (*62*): LOD = SR counts$_{control}$ + 1.645 × SD$_{control}$ + 1.645 × SD$_{min}$, where SD$_{min}$ is the lowest protein concentration in which the mean number of SR counts exceeds its SD. Note that with shape analysis, the probability that a sample would have SR counts ≥1 by chance alone is <3%. To further reduce the false-positive rate for circulating mutant protein detection in clinical samples, we only considered samples to be positive at SR counts >3.

Analysis of protein aggregation

Various GFP-fused mutant p53 (p53^{R175} and p53^{L344P}) or wild-type p53 were expressed in a p53-deficient cell line, BHK21. The concentrations of p53 in the cell lysates were normalized by on denaturing SDS-PAGE. Serial dilutions were performed on the basis of these normalized concentrations. Individual fluorescent spots were initially selected on the first imaging frame using ThunderSTORM for the various p53 protein conformational variants at different concentrations. Because the conformational variants produce spots with distinct intensity distributions, intensity histograms were generated from these spots, and fixed Gaussian fitting was applied to identify curves for different structural populations of p53 (e.g., monomer, dimer, tetramer, and octamer). The areas under the curve for populations greater than or equal to tetramer were integrated and defined as aggregates. The structural compositions of p53 in each sample were hence determined on the basis of the relationship between percentage of aggregates and spot number. Note that although spot number is directly influenced by protein concentration, the relationship between protein concentration and spot number varies depending on p53 conformation (e.g., monomers yield a larger number of imaging spots than aggregates for any given total p53 protein concentration). The spread of intensity distributions allowed us to distinguish among the different p53 variants; mutant p53^{R175H} aggregates had a wider dispersion of fluorescent spot intensities compared to wild-type p53, which likewise had a wider dispersion than mutant p53^{L344P} monomers. We quantified the dispersion of these intensity distributions using the Fano factor, defined as the variance in intensity of an image divided by the mean intensity. The Fano factor serves as an index of aggregation status. For instance, p53^{R175H} complexes showed a higher Fano factor than p53^{L344P} monomers. There was a linear relationship between Fano factor and spot number for all p53 conformational variants, each with distinct slopes. Therefore, by plotting standard curves for Fano factor versus spot number for each of the conformational variants, the aggregation status of p53 could be determined.

Single-molecule anti-p53 autoantibody detection

Recombinant human p53 protein was biotinylated with EZ-Link Sulfo-NHS-Biotin reagent and purified by gel filtration chromatography on 7-kDa columns as described above. Biotinylated protein was stored at −20°C in PBS containing 20% glycerol and 0.1% sodium azide. The purified biotinylated protein was coated in one channel of a dual-channel single-molecule microfluidic capture chip via a streptavidin linker (Thermo Fisher Scientific); the other channel was kept uncoated as a background control. Streptavidin was used instead of NeutrAvidin (a deglycosylated form of avidin protein found in chicken egg white) since most individuals had large amounts of circulating anti-NeutrAvidin IgG, probably because these people eat eggs. Human plasma samples were diluted 10^3 to 10^6 times in SMAC^{BSA} buffer and passed continuously through both channels of the SMAC chip for 2 hours by oscillating flow. The chip was then washed with SMAC^{BSA} buffer (1 ml) and incubated with Alexa Fluor 488–labeled goat anti-human IgG (1 to 10 nM) for 30 min. The chip was washed again and visualized by TIRF microscopy. The spots in the uncoated channel reflected the amount of basal human IgG deposited on the chip via nonspecific binding. Autoantibody levels were hence calculated by subtracting this number of nonspecific IgG counts from total counts in the p53-coated channel.

Quantitative PCR

Serum DNA was extracted with the Plasma/Serum Cell-Free Circulating DNA Purification Micro Kit (Norgen Biotek) according to the manufacturer's instructions. Briefly, 50 μl of mouse serum was collected and eluted with nuclease-free water (50 μl). The eluate (2 μl) was then used for PCR amplification with 2× SsoFast EvaGreen Supermix (Bio-Rad) (10 μl), 5 μM GFP primer mix (2 μl), and nuclease-free water (6 μl) on a CFX96 qPCR system (Bio-Rad) with the following thermal cycling conditions: 98°C for 1 min followed by 60 cycles of 98°C for 5 s and 60°C for 10 s. A melt curve was performed from 65° to 95°C. To generate qPCR standard curves for *gfp* and *p53*, *gfp* and *hp53* plasmid DNA (2 pg), respectively, were serially diluted. Standard curves displayed cycle threshold values as a function of DNA copy number. Primer pairs for p53 qPCR were 5′-CCTTGCCGTCCCAAGCA-3′ (forward) and 5′-

GTGTAGGAGCTGCTGGTG-3′ (reverse). Primer pairs for GFP qPCR were 5′-ACGTAAACGGCCACAAGTTC-3′ (forward) and 5′-AAGTCGTGCTGCTTCATGTG-3′ (reverse).

p53 native protein gel electrophoresis

BHK21 cells were transfected using Lipofectamine 2000 with mutant or wild-type p53 constructs (0.1 to 20 μg of DNA) in six-well plates. After 16 hours, lysate was prepared as described above with 18 mM CHAPS in tris-buffered saline containing deoxyribonuclease and protease inhibitor. Lysate was added with 20% glycerol and 5 mM Coomassie G-250 dye and then loaded onto a 3 to 12% native PAGE bis-tris gel (Invitrogen). Electrophoresis was performed in 50 mM bis-tris and 50 mM tricine plus 0.02% Coomassie G-250 dye in the cathode buffer for 2 hours at 100 V. Proteins were transferred to a polyvinylidene membrane and stained with Coomassie G-250 dye. The membrane was fixed with 8% acetic acid for 20 min and destained with 100% methanol. p53 proteins were detected by immunoblot with DO-1 antibodies and HRP-conjugated anti-mouse secondary antibodies.

Acknowledgments

We are grateful to C. Bohrer and H. Vo for assistance with microfluidic device design and fabrication. We thank T. Ha for helpful advice related to single-molecule imaging. We thank T.C. Wu and B. Vogelstein for insightful input on the manuscript. We thank X. Yang for assistance with TIRF microscope and single-molecule imaging. We thank Y.-C. Tsai for preparing reagents for mice experiments and cell lines. We also thank R. McQuillen and K. Bettridge for helpful discussion. **Funding:** This work was supported by NIH and National Cancer Institute (NIH/NCI) grants 2 P50 CA098252-06, NIH/NCI 2 P50 CA96784-06, NIH/NCI 1 R01 CA114425-06, and NIH/NCI 1 R21 CA194896-01 to C.-F.H. as well as the Johns Hopkins University Discovery Awards and the Hamilton Innovation Award to J.X. C.-P.M. was a recipient of the Ruth L. Kirschstein National Research Service Award (NIH F30 CA177221) and NIH Medical Scientist Training Program Award. S.-C.W. was a recipient of a Taiwanese Government Scholarship. **Author contributions:** C.-P.M., S.-C.W., and C.-F.H. designed the research. C.-P.M., S.-C.W., and Y.-P.S. conducted single-molecule imaging experiments and data processing. Y.-P.S. and S.-H.T. performed mouse experiments and ELISA. L.H. and A.A.W. conducted protein purification. R.B.S.R. supplied human plasma samples. C.-P.M., S.-C.W., R.B.S.R., J.X., and C.-F.H. wrote the paper. **Competing interests:** C.-P.M., S.-C.W., J.X., and C.-F.H. are inventors on two patents related to this work filed by Johns Hopkins University (no. 20190308190, filed 26 September 2017, published 10 October 2019 and no. PCT/US2020/029879, filed 14 August 2018, published 24 April 2020). The other authors declare that they have no competing interest. **Data and materials availability:** All data needed to evaluate the conclusions in the paper are available on the Dataverse repository under DOI https://doi.org/10.7910/DVN/7RIYU8. Correspondence and requests for materials should be addressed to chung2@jhmi.edu.

Supplementary Material

File (sciadv.abg6522_sm.pdf)
DOWNLOAD
View/request a protocol for this paper from *Bio-protocol*.

REFERENCES AND NOTES

D. A. Giljohann, C. A. Mirkin, Drivers of biodiagnostic development. *Nature* **462**, 461–464 (2009).

J. M. Barletta, D. C. Edelman, N. T. Constantine, Lowering the detection limits of HIV-1 viral load using real-time immuno-PCR for HIV-1 p24 antigen. *Am. J. Clin. Pathol.* **122**, 20–27 (2004).

P. R. Srinivas, B. S. Kramer, S. Srivastava, Trends in biomarker research for cancer detection. *Lancet Oncol.* **2**, 698–704 (2001).

D. M. Rissin, C. W. Kan, T. G. Campbell, S. C. Howes, D. R. Fournier, L. Song, T. Piech, P. P. Patel, L. Chang, A. J. Rivnak, E. P. Ferrell, J. D. Randall, G. K. Provuncher, D. R. Walt, D. C. Duffy, Single-

molecule enzyme-linked immunosorbent assay detects serum proteins at subfemtomolar concentrations. *Nat. Biotechnol.* **28**, 595–599 (2010).

J.-M. Nam, C. S. Thaxton, C. A. Mirkin, Nanoparticle-based bio-bar codes for the ultrasensitive detection of proteins. *Science* **301**, 1884–1886 (2003).

S. Fredriksson, W. Dixon, H. Ji, A. C. Koong, M. Mindrinos, R. W. Davis, Multiplexed protein detection by proximity ligation for cancer biomarker validation. *Nat. Methods* **4**, 327–329 (2007).

S. Fredriksson, M. Gullberg, J. Jarvius, C. Olsson, K. Pietras, S. M. Gústafsdóttir, A. Östman, U. Landegren, Protein detection using proximity-dependent DNA ligation assays. *Nat. Biotechnol.* **20**, 473–477 (2002).

V. Ruzicka, W. Marz, A. Russ, W. Gross, Immuno-PCR with a commercially available avidin system. *Science* **260**, 698–699 (1993).

T. Sano, C. L. Smith, C. R. Cantor, Immuno-PCR: Very sensitive antigen detection by means of specific antibody-DNA conjugates. *Science* **258**, 120–122 (1992).

S. Shashkova, M. C. Leake, Single-molecule fluorescence microscopy review: Shedding new light on old problems. *Biosci. Rep.* **37**, BSR20170031 (2017).

A. Jain, R. Liu, B. Ramani, E. Arauz, Y. Ishitsuka, K. Ragunathan, J. Park, J. Chen, Y. K. Xiang, T. Ha, Probing cellular protein complexes using single-molecule pull-down. *Nature* **473**, 484–488 (2011).

A. Jain, R. Liu, Y. K. Xiang, T. Ha, Single-molecule pull-down for studying protein interactions. *Nat. Protoc.* **7**, 445–452 (2012).

P. T. Charles, V. R. Stubbs, C. M. Soto, B. D. Martin, B. J. White, C. R. Taitt, Reduction of non-specific protein adsorption using poly(ethylene) glycol (PEG) modified polyacrylate hydrogels in immunoassays for staphylococcal enterotoxin B detection. *Sensors* **9**, 645–655 (2009).

A. D. Stroock, S. K. Dertinger, A. Ajdari, I. Mezic, H. A. Stone, G. M. Whitesides, Chaotic mixer for microchannels. *Science* **295**, 647–651 (2002).

M. S. Litwin, H.-J. Tan, The diagnosis and treatment of prostate cancer: A review. *JAMA* **317**, 2532–2542 (2017).

F. H. Schröder, J. Hugosson, M. J. Roobol, T. L. J. Tammela, M. Zappa, V. Nelen, M. Kwiatkowski, M. Lujan, L. Määttänen, H. Lilja, L. J. Denis, F. Recker, A. Paez, C. H. Bangma, S. Carlsson, D. Puliti, A. Villers, X. Rebillard, M. Hakama, U.-H. Stenman, P. Kujala, K. Taari, G. Aus, A. Huber, T. H. van der Kwast, R. H. N. van Schaik, H. J. de Koning, S. M. Moss, A. Auvinen; ERSPC Investigators, Screening and prostate cancer mortality: Results of the European Randomised Study of Screening for Prostate Cancer (ERSPC) at 13 years of follow-up. *Lancet* **384**, 2027–2035 (2014).

F. H. Schröder, J. Hugosson, M. J. Roobol, T. L. J. Tammela, S. Ciatto, V. Nelen, M. Kwiatkowski, M. Lujan, H. Lilja, M. Zappa, L. J. Denis, F. Recker, A. Berenguer, L. Määttänen, C. H. Bangma, G. Aus, A. Villers, X. Rebillard, T. van der Kwast, B. G. Blijenberg, S. M. Moss, H. J. de Koning, A. Auvinen; ERSPC Investigators, Screening and prostate-cancer mortality in a randomized European study. *N. Engl. J. Med.* **360**, 1320–1328 (2009).

H. Lilja, D. Ulmert, A. J. Vickers, Prostate-specific antigen and prostate cancer: Prediction, detection and monitoring. *Nat. Rev. Cancer* **8**, 268–278 (2008).

E. M. Genega, B. Hutchinson, V. E. Reuter, P. B. Gaudin, Immunophenotype of high-grade prostatic adenocarcinoma and urothelial carcinoma. *Mod. Pathol.* **13**, 1186–1191 (2000).

F. H. Schröder, I. van der Cruijsen-Koeter, H. J. de Koning, A. N. Vis, R. F. Hoedemaeker, R. Kranse, Prostate cancer detection at low prostate specific antigen. *J. Urol.* **163**, 806–812 (2000).

M. H. Sokoloff, X. J. Yang, M. Fumo, D. Mhoon, C. B. Brendler, Characterizing prostatic adenocarcinomas in men with a serum prostate specific antigen level of < 4.0 ng/mL. *BJU Int.* **93**, 499–502 (2004).

B. A. Mahal, A. A. Aizer, J. A. Efstathiou, P. L. Nguyen, Association of very low prostate-specific antigen levels with increased cancer-specific death in men with high-grade prostate cancer. *Cancer* **122**, 78–83 (2016).

T. Okazaki, S. Chikuma, Y. Iwai, S. Fagarasan, T. Honjo, A rheostat for immune responses: The unique properties of PD-1 and their advantages for clinical application. *Nat. Immunol.* **14**, 1212–1218 (2013).

S. H. Baumeister, G. J. Freeman, G. Dranoff, A. H. Sharpe, Coinhibitory pathways in immunotherapy for cancer. *Annu. Rev. Immunol.* **34**, 539–573 (2016).

D. M. Pardoll, The blockade of immune checkpoints in cancer immunotherapy. *Nat. Rev. Cancer* **12**, 252–264 (2012).

K. E. Brown, G. J. Freeman, E. J. Wherry, A. H. Sharpe, Role of PD-1 in regulating acute infections. *Curr. Opin. Immunol.* **22**, 397–401 (2010).

G. Chen, A. C. Huang, W. Zhang, G. Zhang, M. Wu, W. Xu, Z. Yu, J. Yang, B. Wang, H. Sun, H. Xia, Q. Man, W. Zhong, L. F. Antelo, B. Wu, X. Xiong, X. Liu, L. Guan, T. Li, S. Liu, R. Yang, Y. Lu, L. Dong, S. M. Gettigan, R. Somasundaram, R. Radhakrishnan, G. Mills, Y. Lu, J. Kim, Y. H. Chen, H. Dong, Y. Zhao, G. C. Karakousis, T. C. Mitchell, L. M. Schuchter, M. Herlyn, E. J. Wherry, X. Xu, Exosomal PD-L1 contributes to immunosuppression and is associated with anti-PD-1 response. *Nature* **560**, 382–386 (2018).

J. Zhou, K. M. Mahoney, A. Giobbie-Hurder, F. Zhao, S. Lee, X. Liao, S. Rodig, J. Li, X. Wu, L. H. Butterfield, M. Piesche, M. P. Manos, L. M. Eastman, G. Dranoff, G. J. Freeman, F. S. Hodi, Soluble PD-

L1 as a biomarker in malignant melanoma treated with checkpoint blockade. *Cancer Immunol. Res.* **5**, 480–492 (2017).

D. Gardiner, J. Lalezari, E. Lawitz, M. D. Micco, R. Ghalib, K. R. Reddy, K.-M. Chang, M. Sulkowski, S. O'Marro, J. Anderson, B. He, V. Kansra, F. McPhee, M. Wind-Rotolo, D. Grasela, M. Selby, A. J. Korman, I. Lowy, A randomized, double-blind, placebo-controlled assessment of BMS-936558, a fully human monoclonal antibody to programmed death-1 (PD-1), in patients with chronic hepatitis C virus infection. *PLOS ONE* **8**, e63818 (2013).

J. R. Brahmer, S. S. Tykodi, L. Q. M. Chow, W.-J. Hwu, S. L. Topalian, P. Hwu, C. G. Drake, L. H. Camacho, J. Kauh, K. Odunsi, H. C. Pitot, O. Hamid, S. Bhatia, R. Martins, K. Eaton, S. Chen, T. M. Salay, S. Alaparthy, J. F. Grosso, A. J. Korman, S. M. Parker, S. Agrawal, S. M. Goldberg, D. M. Pardoll, A. Gupta, J. M. Wigginton, Safety and activity of anti–PD-L1 antibody in patients with advanced cancer. *N. Engl. J. Med.* **366**, 2455–2465 (2012).

S. L. Topalian, F. S. Hodi, J. R. Brahmer, S. N. Gettinger, D. C. Smith, D. F. McDermott, J. D. Powderly, R. D. Carvajal, J. A. Sosman, M. B. Atkins, P. D. Leming, D. R. Spigel, S. J. Antonia, L. Horn, C. G. Drake, D. M. Pardoll, L. Chen, W. H. Sharfman, R. A. Anders, J. M. Taube, T. L. McMiller, H. Xu, A. J. Korman, M. Jure-Kunkel, S. Agrawal, D. M. Donald, G. D. Kollia, A. Gupta, J. M. Wigginton, M. Sznol, Safety, activity, and immune correlates of anti-PD-1 antibody in cancer. *N. Engl. J. Med.* **366**, 2443–2454 (2012).

M. Nishino, N. H. Ramaiya, H. Hatabu, F. S. Hodi, Monitoring immune-checkpoint blockade: Response evaluation and biomarker development. *Nat. Rev. Clin. Oncol.* **14**, 655–668 (2017).

R. Roden, T.-C. Wu, How will HPV vaccines affect cervical cancer? *Nat. Rev. Cancer* **6**, 753–763 (2006).

W. Zou, L. Chen, Inhibitory B7-family molecules in the tumour microenvironment. *Nat. Rev. Immunol.* **8**, 467–477 (2008).

O. Saglam, J. Conejo-Garcia, PD-1/PD-L1 immune checkpoint inhibitors in advanced cervical cancer. *Integr. Cancer Sci. Ther.* **5**, 10.15761/ICST.1000272 (2018).

O. L. Reddy, P. I. Shintaku, N. A. Moatamed, Programmed death-ligand 1 (PD-L1) is expressed in a significant number of the uterine cervical carcinomas. *Diagn. Pathol.* **12**, 45 (2017).

M. Polanski, N. L. Anderson, A list of candidate cancer biomarkers for targeted proteomics. *Biomark Insights* **1**, 1–48 (2007).

E. P. Diamandis, The failure of protein cancer biomarkers to reach the clinic: Why, and what can be done to address the problem. *BMC Med.* **10**, 87 (2012).

S.-H. Lee, S.-J. Lee, J.-Y. Chung, Y.-S. Jung, S.-Y. Choi, S.-H. Hwang, D. Choi, N.-C. Ha, B.-J. Park, p53, secreted by K-Ras-Snail pathway, is endocytosed by K-Ras-mutated cells; Implication of target-specific drug delivery and early diagnostic marker. *Oncogene* **28**, 2005–2014 (2009).

Q. Wang, R. Chaerkady, J. Wu, H. J. Hwang, N. Papadopoulos, L. Kopelovich, A. Maitra, H. Matthaei, J. R. Eshleman, R. H. Hruban, K. W. Kinzler, A. Pandey, B. Vogelstein, Mutant proteins as cancer-specific biomarkers. *Proc. Natl. Acad. Sci. U.S.A.* **108**, 2444–2449 (2011).

K.-Y. Lin, F. G. Guarnieri, K. F. Staveley-O'Carroll, H. I. Levitsky, J. T. August, D. M. Pardoll, T.-C. Wu, Treatment of established tumors with a novel vaccine that enhances major histocompatibility class II presentation of tumor antigen. *Cancer Res.* **56**, 21–26 (1996).

C. M. Carlson, J. L. Frandsen, N. Kirchhof, R. S. McIvor, D. A. Largaespada, Somatic integration of an oncogene-harboring *Sleeping Beauty* transposon models liver tumor development in the mouse. *Proc. Natl. Acad. Sci. U.S.A.* **102**, 17059–17064 (2005).

M. Ignatiadis, G. W. Sledge, S. S. Jeffrey, Liquid biopsy enters the clinic – Implementation issues and future challenges. *Nat. Rev. Clin. Oncol.* **18**, 297–312 (2021).

A. M. Lennon, A. H. Buchanan, I. Kinde, A. Warren, A. Honushefsky, A. T. Cohain, D. H. Ledbetter, F. Sanfilippo, K. Sheridan, D. Rosica, C. S. Adonizio, H. J. Hwang, K. Lahouel, J. D. Cohen, C. Douville, A. A. Patel, L. N. Hagmann, D. D. Rolston, N. Malani, S. Zhou, C. Bettegowda, D. L. Diehl, B. Urban, C. D. Still, L. Kann, J. I. Woods, Z. M. Salvati, J. Vadakara, R. Leeming, P. Bhattacharya, C. Walter, A. Parker, C. Lengauer, A. Klein, C. Tomasetti, E. K. Fishman, R. H. Hruban, K. W. Kinzler, B. Vogelstein, N. Papadopoulos, Feasibility of blood testing combined with PET-CT to screen for cancer and guide intervention. *Science* **369**, eabb9601 (2020).

T. J. Sweeney, V. Mailänder, A. A. Tucker, A. B. Olomu, W. Zhang, Y. Cao, R. S. Negrin, C. H. Contag, Visualizing the kinetics of tumor-cell clearance in living animals. *Proc. Natl. Acad. Sci. U.S.A.* **96**, 12044–12049 (1999).

A. J. Levine, M. Oren, The first 30 years of p53: Growing ever more complex. *Nat. Rev. Cancer* **9**, 749–758 (2009).

P. A. J. Muller, K. H. Vousden, p53 mutations in cancer. *Nat. Cell Biol.* **15**, 2–8 (2013).

P. A. J. Muller, K. H. Vousden, Mutant p53 in cancer: New functions and therapeutic opportunities. *Cancer Cell* **25**, 304–317 (2014).

The Cancer Genome Atlas Research Network, Integrated genomic analyses of ovarian carcinoma. *Nature* **474**, 609–615 (2011).

T. Soussi, p53 Antibodies in the sera of patients with various types of cancer: A review. *Cancer Res.* **60**, 1777–1788 (2000).

R. T. Fortner, H. Schock, C. L. Cornet, A. Hüsing, A. F. Vitonis, T. S. Johnson, R. N. Fichorova, T. Fashemi, H. S. Yamamoto, A. Tjønneland, L. Hansen, K. Overvad, M.-C. Boutron-Ruault, M. Kvaskoff, G. Severi, H. Boeing, A. Trichopoulou, E.-M. Papatesta, C. L. Vecchia, D. Palli, S. Sieri, R. Tumino, C. Sacerdote, A. Mattiello, N. C. Onland-Moret, P. H. Peeters, H. Bueno-de-Mesquita, E. Weiderpass, J. R. Quirós, E. J. Duell, M.-J. Sánchez, C. Navarro, E. Ardanaz, N. Larrañaga, B. Nodin, K. Jirström, A. Idahl, E. Lundin, K.-T. Khaw, R. C. Travis, M. Gunter, M. Johansson, L. Dossus, M. A. Merritt, E. Riboli, K. L. Terry, D. W. Cramer, R. Kaaks, Ovarian cancer early detection by circulating CA125 in the context of anti-CA125 autoantibody levels: Results from the EPIC cohort. *Int. J. Cancer* **142**, 1355–1360 (2018).

A. E. Lokshin, M. Winans, D. Landsittel, A. M. Marrangoni, L. Velikokhatnaya, F. Modugno, B. M. Nolen, E. Gorelik, Circulating IL-8 and anti-IL-8 autoantibody in patients with ovarian cancer. *Gynecol. Oncol.* **102**, 244–251 (2006).

J. D. Cohen, L. Li, Y. Wang, C. Thoburn, B. Afsari, L. Danilova, C. Douville, A. A. Javed, F. Wong, A. Mattox, R. H. Hruban, C. L. Wolfgang, M. G. Goggins, M. D. Molin, T.-L. Wang, R. Roden, A. P. Klein, J. Ptak, L. Dobbyn, J. Schaefer, N. Silliman, M. Popoli, J. T. Vogelstein, J. D. Browne, R. E. Schoen, R. E. Brand, J. Tie, P. Gibbs, H.-L. Wong, A. S. Mansfield, J. Jen, S. M. Hanash, M. Falconi, P. J. Allen, S. Zhou, C. Bettegowda, L. A. Diaz Jr., C. Tomasetti, K. W. Kinzler, B. Vogelstein, A. M. Lennon, N. Papadopoulos, Detection and localization of surgically resectable cancers with a multi-analyte blood test. *Science* **359**, 926–930 (2018).

L. A. Torre, B. Trabert, C. E. DeSantis, K. D. Miller, G. Samimi, C. D. Runowicz, M. M. Gaudet, A. Jemal, R. L. Siegel, Ovarian cancer statistics, 2018. *CA Cancer J. Clin.* **68**, 284–296 (2018).

G. Wang, A. R. Fersht, Multisite aggregation of p53 and implications for drug rescue. *Proc. Natl. Acad. Sci. U.S.A.* **114**, E2634–E2643 (2017).

J. F. R. Kerr, A. H. Wyllie, A. R. Currie, Apoptosis: A basic biological phenomenon with wide-ranging implications in tissue kinetics. *Br. J. Cancer* **26**, 239–257 (1972).

S. Sperandio, I. de Belle, D. E. Bredesen, An alternative, nonapoptotic form of programmed cell death. *Proc. Natl. Acad. Sci. U.S.A.* **97**, 14376–14381 (2000).

L. M. Schwartz, S. W. Smith, M. E. Jones, B. A. Osborne, Do all programmed cell deaths occur via apoptosis? *Proc. Natl. Acad. Sci. U.S.A.* **90**, 980–984 (1993).
J. Debnath, E. H. Baehrecke, G. Kroemer, Does autophagy contribute to cell death? *Autophagy* **1**, 66–74 (2005).

D. Gozuacik, A. Kimchi, Autophagy as a cell death and tumor suppressor mechanism. *Oncogene* **23**, 2891–2906 (2004).

M. Ovesný, P. Křížek, J. Borkovec, Z. Švindrych, G. M. Hagen, ThunderSTORM: A comprehensive ImageJ plug-in for PALM and STORM data analysis and super-resolution imaging. *Bioinformatics* **30**, 2389–2390 (2014).

D. A. Armbruster, T. Pry, Limit of blank, limit of detection and limit of quantitation. *Clin. Biochem. Rev.* **29** (Suppl. 1), S49–S52 (2008).